

The Heavy Photon Search Test Detector

M. Battaglieri^a, S. Boyarinov^b, S. Buelmann^c, V. Burkert^b, G. Charles^d, W. Cooper^e, N. Dashyan^f, R. De Vita^a, A. Deur^b, R. Dupre^d, H. Egiyan^b, L. Elouadrhiri^b, R. Essig^g, V. Fadeyev^h, C. Fieldⁱ, A. Freyberger^b, N. Gevorgyan^f, F.-X. Girod^b, N. Grafⁱ, M. Grahamⁱ, K. Griffioen^j, A. Grillo^h, M. Guidal^d, G. Hallerⁱ, P. Hansson Adrian^{i,*}, R. Herbstⁱ, M. Holtrop^k, J. Jarosⁱ, S. K. Phillips^k, M. Khandaker^l, A. Kubarovskiy^m, T. Maruyamaⁱ, J. McCormickⁱ, K. Moffeitⁱ, O. Moreno^h, H. Nealⁱ, T. Nelsonⁱ, S. Niccolai^d, A. Odianⁱ, M. Oriunnoⁱ, R. Paremuzyan^f, E. Rauly^d, E. Rindel^d, P. Rosier^d, C. Salgado^l, P. Schusterⁿ, Y. Sharabian^b, K. Slifer^k, D. Sokhan^o, S. Stepanyan^b, P. Stoler^m, N. Toroⁿ, S. Uemuraⁱ, M. Ungaro^b, H. Voskanyan^f, D. Walzⁱ, L. B. Weinstein^c, B. Wojtsekowski^b

^aIstituto Nazionale di Fisica Nucleare, Sezione di Genova e Dipartimento di Fisica dell'Università, 16146 Genova, Italy

^bThomas Jefferson National Accelerator Facility, Newport News, Virginia 23606

^cOld Dominion University, Norfolk, Virginia 23529

^dInstitut de Physique Nucléaire d'Orsay, IN2P3, BP 1, 91406 Orsay, France

^eFermi National Accelerator Laboratory, Batavia, IL 60510-5011

^fYerevan Physics Institute, 375036 Yerevan, Armenia

^gStony Brook University, Stony Brook, NY 11794-3800

^hUniversity of California, Santa Cruz, CA 95064

ⁱSLAC National Accelerator Laboratory, Menlo Park, CA 94025

^jThe College of William and Mary, Department of Physics, Williamsburg, VA 23185

^kUniversity of New Hampshire, Department of Physics, Durham, NH 03824

^lNorfolk State University, Norfolk, Virginia 23504

^mRensselaer Polytechnic Institute, Department of Physics, Troy, NY 12181

ⁿPerimeter Institute, Ontario, Canada N2L 2Y5

^oUniversity of Glasgow, Glasgow, G12 8QQ, Scotland, UK

Abstract

The Heavy Photon Search (HPS), an experiment to search for a hidden sector photon in fixed target electroproduction, is preparing for installation at the Thomas Jefferson National Accelerator Facility (JLab) in the Fall of 2014. As the first stage of this project, the HPS Test Run apparatus was constructed and operated in 2012 to demonstrate the experiment's technical feasibility and to confirm that the trigger rates and occupancies are as expected. This paper describes the HPS Test Run apparatus and readout electronics and its performance. In this setting, a heavy photon can be identified as a narrow peak in the e^+e^- invariant mass spectrum, above the trident background or as a narrow invariant mass peak with a decay vertex displaced from the production target, so charged particle tracking and vertexing are needed for its detection. In the HPS Test Run, charged particles are measured with a compact forward silicon microstrip tracker inside a dipole magnet. Electromagnetic showers are detected in a PbWO₄ crystal calorimeter situated behind the magnet used to trigger the experiment and identify electrons and positrons. Both detectors are placed close to the beam line and split top-bottom. This arrangement provides sensitivity to low-mass heavy photons, allows clear passage of the unscattered beam, and avoids the spray of degraded electrons coming from the target. The discrimination between prompt and displaced e^+e^- pairs requires the first layer of silicon sensors be placed only 10 cm downstream of the target. The expected signal is small, and the trident background huge, so the experiment requires very large statistics. Accordingly, the HPS Test Run utilizes high-rate readout and data acquisition electronics and a fast trigger to exploit the essentially 100% duty cycle of the CEBAF accelerator at JLab.

Keywords: silicon microstrip, tracking, vertexing, heavy photon, dark photon, hidden sector, electromagnetic calorimeter

*Corresponding author.

Email address: phansson@slac.stanford.edu (P. Hansson)

Adrian)

1 **Contents**

2	1	Introduction	3
3	2	Detector Overview	3
4	3	The HPS Test Run Beamline	5
5	4	Silicon Vertex Tracker	5
6	4.1	Layout	6
7	4.2	Components	6
8	4.3	Production, Assembly and Shipping . .	7
9	4.4	Alignment	7
10	5	Electromagnetic Calorimeter	8
11	5.1	Components	8
12	5.2	Layout	8
13	5.3	Signal readout	8
14	6	Trigger and Data Acquisition	9
15	6.1	Trigger system	9
16	6.2	SVT Data Acquisition	9
17	6.3	General Data Acquisition and Online Computing	10
19	7	Reconstruction and Performance	10
20	7.1	SVT Performance	10
21	7.1.1	Cluster and Hit Reconstruction .	11
22	7.1.2	Momentum and Vertexing Res- olution	11
23	7.2	ECal Performance	12
24	7.3	Trigger Performance	14
25	7.4	Trigger Rate Comparisons	14
27	8	Summary and Outlook	14
28	9	Acknowledgements	15

29 **1. Introduction**

30 The heavy photon (A'), aka a “hidden sector” or
31 “dark” photon, is a particle with mass $10 - 1000 \text{ MeV}/c^2$
32 which couples weakly to electric charge by mixing with
33 the Standard Model photon [1]. Consequently, it can
34 be radiated by electrons and subsequently decay into
35 e^+e^- pairs, albeit at rates far below those of QED trident
36 processes. Heavy photons have been suggested by nu-
37 merous beyond Standard Model theories [2], to explain
38 the discrepancy between theory and experiment of the
39 muon’s $g - 2$ [3], and as a possible explanation of recent
40 astrophysical anomalies [4, 5, 6]. Heavy photons couple
41 directly to hidden sector particles with “dark” or “hid-
42 den sector” charge; these particles could constitute all
43 or some of the dark matter [7]. Current phenomenology
44 highlights the $20 - 1000 \text{ MeV}/c^2$ mass range, and sug-
45 gests that the coupling to electric charge, ϵe , has ϵ in the
46 range of $10^{-3} - 10^{-5}$. This range of parameters makes
47 A' searches viable in medium energy fixed target elec-
48 troproduction [8], but requires large data sets and good
49 mass resolution to identify a small mass peak above the
50 copious QED background. At small couplings, A' be-
51 come long-lived, so detection of a displaced decay ver-
52 tex can reject the prompt QED background and boost
53 experimental sensitivity.

54 The HPS experiment [9] uses both invariant mass and
55 secondary vertex signatures to search for A' . It uses a
56 $\approx 1 \text{ m}$ long silicon tracking and vertexing detector in-
57 side a dipole magnet to measure charged particle trajec-
58 tories and a fast electromagnetic calorimeter just down-
59 stream of the magnet to provide a trigger and identify
60 electrons. The experiment utilizes very high-rate front-
61 end electronics and runs at high trigger rates (up to
62 50kHz), exploiting the 100% duty cycle of the JLab CE-
63 BAF accelerator to accumulate the needed statistics.

64 The HPS Test Run, using a simplified version of the
65 HPS apparatus, was proposed and approved at JLab as
66 the first stage of HPS. Its purposes included demon-
67 strating that the apparatus and data acquisition systems are
68 technically feasible and the trigger rates and occupan-
69 cies to be encountered in electron-beam running are as
70 simulated. Given dedicated running time with electron
71 beams, the HPS Test Run apparatus is capable of search-
72 ing for heavy photons in unexplored regions of parame-
73 ter space. The key design criteria for HPS and the HPS
74 Test Run are the same:

- 75 • large and uniform acceptance in the forward region
76 close to the beam in order to catch boosted A' de-
77 cay products,
- 78 • beam passage through the apparatus in vacuum, to

79 eliminate direct interactions with the detector and
80 minimize beam gas interactions,

- 81 • detector components that can survive and effi-
82 ciently operate in a high radiation environment
83 with local doses exceeding 100 Mrad.
- 84 • high-rate electronics with excellent timing resolu-
85 tion to minimize out of time backgrounds,
- 86 • a flexible, redundant and efficient trigger selecting
87 electron and positron pairs at rates up to 50 kHz,
- 88 • data handling rates of 100 MB/s to permanent stor-
89 age,
- 90 • excellent track reconstruction efficiency for elec-
91 trons and positrons,
- 92 • good angular and momentum resolution to recon-
93 struct invariant mass precisely,
- 94 • excellent vertex resolution to discriminate dis-
95 placed A' decays from prompt QED backgrounds,

96 The HPS Test Run apparatus was installed on April
97 19, 2012, and ran parasitically in the photon beam of
98 the HDice experiment [10] until May 18. The JLab
99 run schedule precluded any dedicated electron beam
100 running, but the HPS Test Run was allowed a short
101 and valuable dedicated photon beam run at the end of
102 scheduled CEBAF running. This final running provided
103 enough data to demonstrate the functionality of the ap-
104 paratus, document its performance, and explore trigger
105 rates, as shown below.

106 This paper reviews the HPS Test Run apparatus, doc-
107 umenting the performance of the trigger, data acqui-
108 sition, silicon tracking detector, and the electromag-
109 netic calorimeter at the level required for calculating the
110 physics reach of the HPS experiment.

111 **2. Detector Overview**

112 The HPS Test Run apparatus was designed to run
113 in Hall B at JLab using the CEBAF 499MHz electron
114 beam at energies between 2.2 and 6.6 GeV and cur-
115 rents between 200 and 600 nA. The overall design of
116 the experiment follows from the kinematics of A' pro-
117 duction which typically results in a final state particle
118 within a few degrees of the incoming beam, especially
119 at low $m_{A'}$. Detectors must therefore be placed close
120 to the beam. The intense electron beam enlarges down-
121 stream after multiple scattering in the target and elec-
122 trons which have radiated in the target disperse horizon-
123 tally in the field of the analyzing magnet. Together they

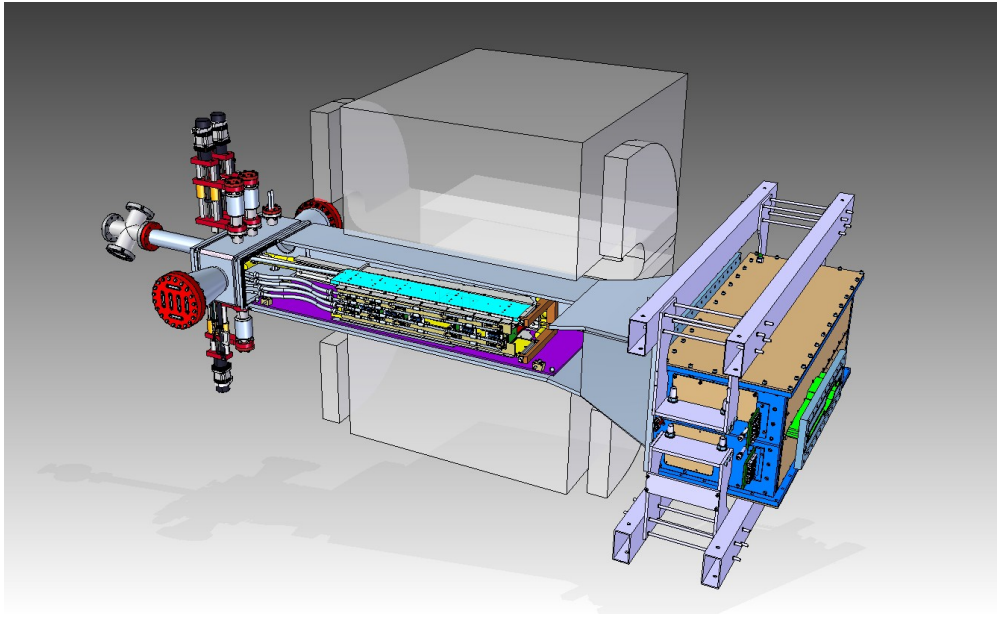


Figure 1: Rendering of the HPS Test Run apparatus installed on the beam line.

124 constitute a “wall of flame” which must be completely
 125 avoided. Accordingly, the apparatus is split vertically
 126 to avoid a “dead zone”, the region within ± 15 mrad of
 127 the beam plane. In addition, the beam is transported in
 128 vacuum through the tracker to minimize beam-gas inter-
 129 action backgrounds. Even with these precautions, the
 130 occupancies of sensors near the beam plane are high,
 131 dominated by the multiple Coulomb scattering of the
 132 primary beam, so high-rate detectors, a fast trigger, and
 133 excellent time tagging are required to minimize their
 134 impact. The trigger comes from a highly-segmented
 135 lead-tungstate (PbWO_4) crystal calorimeter located just
 136 downstream of the dipole magnet.

137
 138 A rendering of the apparatus installed on the beam line
 139 is shown in Figure 1 and an overview of the coverage,
 140 segmentation and performance is given in Table 1.

141 The silicon vertex tracking and vertexing detector for
 142 the HPS Test Run, or SVT, resides in a vacuum cham-
 143 ber inside the Pair Spectrometer (PS) dipole magnet in
 144 Hall B at JLab. The magnetic field strength was 0.5 T
 145 oriented vertically throughout the run. The SVT has
 146 five measurement stations, or “layers,” beginning 10 cm
 147 downstream of the target. Each layer comprises a pair
 148 of closely-spaced silicon microstrip sensors responsi-
 149 ble for measuring a single coordinate, or “view”. In-
 150 troduction of a small (50 or 100 mrad) stereo angle

151 between the two sensors of each layer provides three-
 152 dimensional tracking and vertexing throughout the ac-
 153 ceptance of the detector. In order to accommodate the
 154 dead zone, the SVT is built in two halves that are ap-
 155 proximately mirror reflections of one another about the
 156 plane of the nominal electron beam. Each layer in one
 157 half is supported on a common support plate with inde-
 158 pendent cooling and readout.

159
 160 The electromagnetic calorimeter (ECal) is also split
 161 into two halves. Each half of the ECal consists of
 162 221 PbWO_4 crystals arranged in rectangular formation.
 163 There are five rows with 46 modules in each row except
 164 the row closest to the beam plane which has 37. The
 165 light from each crystal is read out by an Avalanche Pho-
 166 todioide (APD) glued on the back surface of the crys-
 167 tal. Signals from the APDs are amplified using custom-
 168 made amplifier boards before being sent to the data ac-
 quisition electronics.

169 The Data Acquisition system combines two architec-
 170 tures, the Advanced Telecom Communications Archi-
 171 tecture (ATCA) based SVT readout system and VME-
 172 bus Switched Serial (VXS) based digitization and trig-
 173 gering system for the ECal. The system was designed
 174 to run at up to 20 kHz trigger rate.

Table 1: Overview of the coverage, segmentation and performance of the HPS Test Run detector.

System	Coverage (mrad)	# channels	ADC (bit)	Time resolution (ns)	# layers	Segmentation	Performance
SVT	$15 < \theta_y < 70$ (5 hits)	12780	14	≈ 2 ns	5 (stereo layers)	$\approx 120 \mu\text{m} r - \phi$ $\approx 6 \mu\text{m} z$	$\sigma_{d0,y} \approx 100 \mu\text{m}$ $\sigma_{d0,x} \approx 300 \mu\text{m}$ $\sigma_{d0,z} \approx 1 \text{ mm}$
Ecal	$15 < \theta_y < 60$	442	12	4 ns	1	$1.33 \times 1.33 \text{ cm}^2$ $1.6 \times 1.6 \text{ cm}^2$	$\sigma(E)/E \approx 4.5\%$

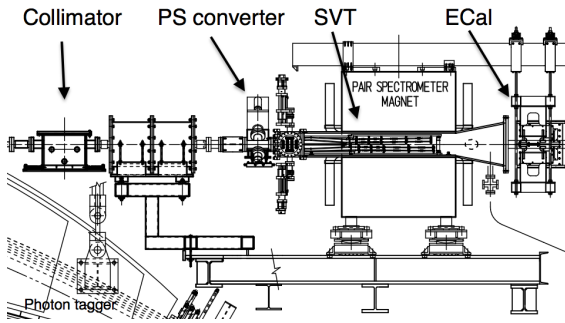


Figure 2: Layout of the HPS parasitic run.

175 3. The HPS Test Run Beamline

176 Since an electron beam was unavailable, the HPS Test
 177 Run detected the electrons and positrons produced by
 178 interactions of the secondary photon beam with a thin
 179 foil just upstream of the detectors. The HPS Test Run
 180 studied the performance of the detectors and the mul-
 181 tiple coulomb scattering of the electrons and positrons.
 182 Figure 2 shows the layout of the setup on the beam line.
 183 The SVT was installed inside the Hall B pair spectrom-
 184 ete magnet vacuum chamber with the ECal mounted
 185 downstream of it. Both the SVT and the ECal were re-
 186 tracted off the beam plane compared to nominal electron
 187 beam running to allow clean passage of the photon beam
 188 through the system.

189 The photon beam was generated in the interaction of
 190 5.5 GeV electrons with a $10^{-4} X_0$ gold radiator located
 191 ≈ 9 m upstream of the PS. The primary beam and scat-
 192 tered electrons are deflected away from detectors by the
 193 dipole magnet of the photon tagging system. During the
 194 dedicated HPS Test Run period, the collimated (6.4 mm
 195 diameter) photon beam passes through the PS pair con-
 196 verter gold foil and later the HPS system. The PS pair
 197 converter was located ≈ 77 cm upstream of the first
 198 layer of the SVT.

199 Data was taken on three different converter thick-
 200 nesses with photon fluxes between 0.4 and $1.3 \times 10^8/\text{s}$
 201 at photon energies between 0.55 and 5.5 GeV produced
 202 by a 30 to 90 nA electron beam. Data was measured

Converter thickn. (% X_0)	Duration (s)	e^- on radiator (μC)
0	1279	88.1
0.18	2640	193.5
0.45	2149	140.7
1.6	911	24.4

Table 2: Measured integrated currents for the dedicated photon runs.

203 for both polarities of the PS dipole magnet.’ The photon
 204 beam line during the HPS Test Run produced a rela-
 205 tively large number of e^+e^- pairs originating upstream
 206 of the converter position. This contribution was mea-
 207 sured during data taking with “empty” converter runs,
 208 i.e. removing the converter but with all other conditions
 209 the same. The runs taken during the time dedicated to
 210 HPS Test Run are summarized in Table 2.

211 4. Silicon Vertex Tracker

212 The Silicon Vertex Tracker (SVT) enables efficient
 213 reconstruction of charged particles and precise determi-
 214 nation of their trajectories. These measurements allow
 215 A' decays to be distinguished from background via sim-
 216 ultaneous estimation of the invariant mass of e^+e^- de-
 217 cay products and the position of decay vertices down-
 218 stream of the target.

219 The design of the SVT is primarily driven by direct
 220 physics requirements and constraints from the environ-
 221 ment at the interaction region. The A' decay products
 222 have momenta in the range of 1 GeV, so multiple scat-
 223 tering dominates mass and vertexing uncertainties for
 224 any possible material budget. The SVT must therefore
 225 minimize the amount of material in the tracking vol-
 226 ume. The signal yield for long-lived A' is very small,
 227 so the rejection of prompt vertices must be exceedingly
 228 pure, on the order of 10^{-7} , in order to eliminate all
 229 prompt backgrounds. To achieve the required vertexing
 230 performance the first layer of the SVT must be placed
 231 no more than about 10 cm downstream of the target.
 232 At that distance, it is found that the active region of

233 a sensor can be placed as close as 1.5 mm from the 260
 234 center of the beam, defining the 15 mrad “dead zone”
 235 mentioned previously, to maximize low-mass A’ ac- 261
 236 ceptance with decay products nearly collinear with the 262
 237 beam axis. At the edge of this “dead zone”, the radiation 263
 238 dose approaches 10^{15} electrons/cm²/month, or roughly 264
 239 3×10^{14} 1 MeV neutron equivalent/cm²/month [11], re- 265
 240 quiring the sensors to be actively cooled. Meanwhile, 266
 241 very low-energy delta rays from beam-gas interactions 267
 242 multiply the density of background hits, so the SVT 268
 243 must operate inside the beam vacuum. Finally, in 269
 244 order to protect the sensors, the detector must be movable 270
 245 so that it can be retracted during periods of uncertain 271
 246 beam conditions. 272
 247

4.1. Layout

The layout of the SVT is summarized in Table 4.1 and 248
 rendered in Figure 3. Each of the layers is comprised 249
 of a pair of closely-spaced silicon microstrip sensors 250
 mounted back-to-back to form a module. A 100 mrad 251
 stereo angle is used in the first three layers to provide 252
 higher-resolution 3D space points for vertexing. Using 253
 50 mrad in the last two layers breaks the tracking de- 254
 generacy of having five identical layers and minimizes 255
 fakes from ghost hits to improve pattern recognition. 256
 Altogether, the SVT has 20 sensors for a total of 12780 257
 readout channels. 258

Layer	1	2	3	4	5
<i>z</i> from target (cm)	10	20	30	50	70
Stereo angle (mrad)	100	100	100	50	50
Bend res. (μm)	≈ 60	≈ 60	≈ 60	≈ 120	≈ 120
Non-bend res. (μm)	≈ 6	≈ 6	≈ 6	≈ 6	≈ 6
# of sensors	4	4	4	4	4
Dead zone (mm)	± 1.5	± 3.0	± 4.5	± 7.5	± 10.5
Power cons. (W)	6.9	6.9	6.9	6.9	6.9

Table 3: Layout of the SVT.

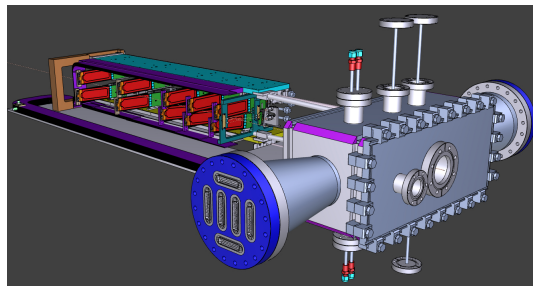


Figure 3: A rendering of the SVT showing the modules on their 277
 support plates held by the hinged C-support on the left and the 278
 motion levers on the right. The sensors are shown in red and 279
 the hybrid readout boards in green. The beam enters from the 280
 right through a vacuum box with flanges for services. 281
 282

The SVT is built in two separate halves that are mirror 261
 reflections of one another about the plane of the nomi- 262
 nal electron beam. Each half consists of five modules 263
 mounted on a support plate that provides services to the 264
 modules and allows them to be moved as a group rela- 265
 tive to the dead zone. The two halves of the tracker 266
 are connected to hinges mounted on a C-shaped support 267
 just beyond the last layer that defines the nominal spac- 268
 ing between the upper and lower halves of the tracker. 269
 A shaft attached to each support plate in front of layer 270
 one extends upstream and connects to a linear shift that 271
 transfers motion into the vacuum box through bellows 272
 to open and close the two halves around the dead zone. 273
 The C-support is mounted to an aluminum baseplate 274
 that defines the position of the SVT with respect to the 275
 vacuum chamber. Figure 4 shows a photograph of both 276
 completed detector halves prior to final assembly.



Figure 4: Both halves of the HPS Test Run SVT after final 277
 assembly at SLAC. The cooling manifolds and integrated 278
 cable runs are clearly seen.

4.2. Components

The sensors for the SVT are *p*-on-*n*, single-sided, 279
 AC-coupled, polysilicon-biased microstrip sensors fab- 280
 ricated on <100> silicon and have 30 (60) μm sense 281
 (readout) pitch over their $4 \times 10 \text{ cm}^2$ surface. This 282
 sensor technology was selected to match the require- 283
 ment of $< 1\% X_0$ per layer, single-hit resolution bet- 284
 ter than 50 μm and tolerance of a radiation dose of ap- 285
 proximately 1.5×10^{14} 1 MeV neutron equivalent/cm² 286
 for a six month run. The sensors were purchased from 287
 the Hamamatsu Photonics Corporation for the cancelled 288
 Run 2b upgrade of the DØ experiment [12] which satis- 289
 fied the requirement that the technology must be mature 290
 and available within the time and budget constraints.

Despite having only small spots with very high occupancy (up to 4 MHz/mm^2) closest to the primary beam, the rates are still high and lowering the peak occupancy to approximately 1% for tracking requires a trigger window and hit time tagging of roughly 8 ns. The ECal readout and trigger described in Sec. 5.3 can achieve such resolution. To reach this performance the sensors for the SVT are readout by the APV25 ASIC developed for the CMS experiment at CERN [13]. The APV25 can capture successive samples of the shaper output in groups of three at a sampling rate of approximately 40 MHz. By fitting the known *CR-RC* shaping curve to these samples, the initial time of the hit can be determined to a precision of 2 ns for $S/N \approx 25$ [14]. For electron beam running, six-sample readout and the shortest possible shaping time (35 ns) is used to best distinguish hits that overlap in time. The APV25 ASICs are hosted on simple FR4 hybrid readout boards, outside the tracking volume, with a short twisted-pair pigtail cable to provide power and configuration and signal readout. Along with a single sensor, these are glued to a polyamide-laminated carbon fiber composite backing making up a half-module. A window is machined in the carbon fiber leaving only a frame around the periphery of the silicon to minimize material. A $50 \mu\text{m}$ sheet of polyamide is laminated to the surface of the carbon fiber with 1 mm overhang at all openings to ensure good isolation between the back side of the sensor, carrying high-voltage bias, and the carbon fiber which is held near ground.

The sensor modules for the SVT consist of a pair of identical half-modules, sandwiched back-to-back around an aluminum cooling block at one end and a similar PEEK spacer block at the other. Figure 5 shows a single module after assembly. The cooling block pro-

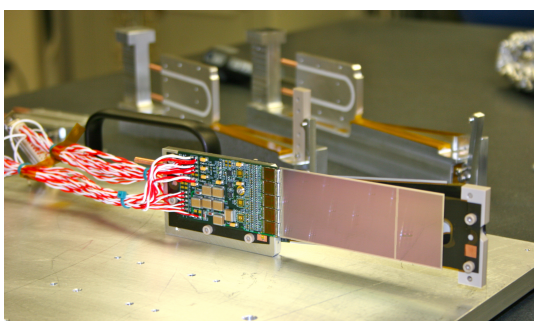


Figure 5: A prototype module assembly (foreground) with the 50 mrad (left) and 100 mrad (right) module assembly fixtures in the background. A pair of cooling blocks and a spacer block can be seen on the fixtures.

vides the primary mechanical support for the module as

well as cooling via copper tubes pressed into grooves in the plates. The spacer block defines the spacing between the sensors at the far end of the module, stiffens the module structure, and improves the stability of the sensor alignment. The average support material in the tracking volume is approximately $0.06\% X_0$ per double-sided module for a total material budget of 0.7% per layer.

The total SVT power consumption budget of about 50 W is removed by a water/glycol mixture circulated through a flexible manifold attached to the copper tubes in the cooling blocks. During the HPS Test Run the sensors were operated at around 23°C . The power consumption is dominated by five APV25 ASICs on each hybrid board consuming approximately 2 W, radiant heat load is less than 0.5 W per sensor and leakage current is only significant in a small spot after irradiation.

4.3. Production, Assembly and Shipping

Hybrids with APV25 ASICs underwent quick qualification testing and each half-module was run at low temperature ($\approx 5^\circ \text{C}$) and fully characterized for pedestals, gains, noise and time response after assembly. Of 29 half-modules built, 28 passed qualification testing, leaving eight spare modules after completion of the SVT. Only sensors capable of 1000 V bias voltage without breakdown were used. Full-module assembly and mechanical surveys were performed at SLAC before final assembly, testing and shipping of the SVT to JLab. A custom shipping container with nested crates and redundant isolation for shock and vibration was built in order to safely send the partly assembled SVT to JLab. At JLab, the entire SVT was integrated with the full DAQ and the power supplies before moving the module-loaded support plates to Hall B for final mechanical assembly and installation inside of the vacuum chamber.

4.4. Alignment

The SVT was aligned using a combination of optical, laser and touch probe surveys at SLAC and JLab. The optical survey of individual modules with a precision of a few μm was combined with a touch-probe survey of the overall SVT support structure, with 25-100 μm precision, to locate the silicon sensor layers with respect to the support plates and the mechanical survey balls on the base plate. After full assembly and installation of the SVT at JLab, a mechanical survey of the SVT base plate position inside the pair spectrometer vacuum chamber is used to determine the global position of the SVT with respect to the CEBAF beam line. The resulting survey-based alignment has the position of the

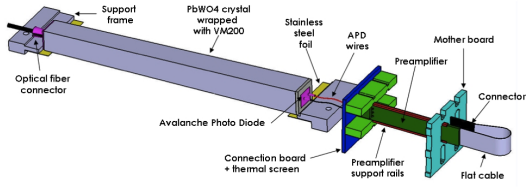


Figure 6: A schematic view of an ECal module.

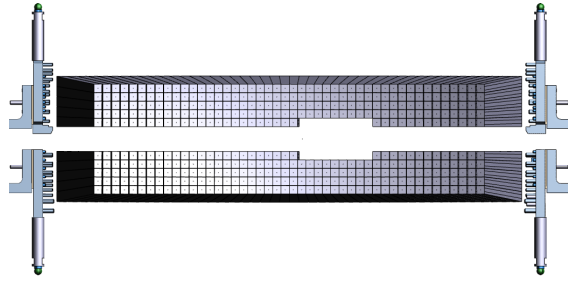


Figure 7: Rendered layout view of the ECal looking downstream.

377 silicon sensors correct to within a few hundred microns
 378 measured from tracks in the HPS Test Run data. A more
 379 sophisticated global track-based alignment technique to
 380 reach final alignment precision well below $50\text{ }\mu\text{m}$ is be-
 381 ing developed.

382 5. Electromagnetic Calorimeter

383 The electromagnetic calorimeter (ECal), installed
 384 downstream of the PS dipole magnet, performs two es-
 385 sential functions for the experiment: it provides a trigger
 386 signal to select what events to read out from the detector
 387 sub-systems and is used in the analysis to identify elec-
 388 trons and positrons. The technology and design choices
 389 are largely driven by the need for a compact forward de-
 390 sign covering the SVT A' acceptance and able to fully
 391 absorb electrons and positrons with energy between 0.5-
 392 6.5 GeV. It needs granularity and signal readout speed to
 393 handle $1\text{ MHz}/\text{cm}^2$ of electromagnetic background and
 394 be radiation hard. The PbWO₄ crystal inner calorime-
 395 ter of the CLAS detector [15], in operation since 2005
 396 in Hall B, meets all the requirements set by HPS. The
 397 modules from this calorimeter have been subsequently
 398 repurposed for HPS.

399 5.1. Components

400 The ECal module shown in Figure 6 is based on a
 401 tapered 160 mm long PbWO₄ crystal with a $13.3 \times$
 402 13.3 mm^2 ($16 \times 16\text{ mm}^2$) front (rear) face wrapped in
 403 VM2000 multilayer polymer mirror film. The scintilla-
 404 tion light, approximately 3 photoelectrons/MeV, is read
 405 out by a $5 \times 5\text{ mm}^2$ Hamamatsu S8664-55 Avalanche
 406 Photodiode (APD) with 75% quantum efficiency glued
 407 to the rear face surface using MeltMount 1.7 thermal
 408 plastic adhesive. The low gain of APDs (~ 200) was
 409 compensated with custom-made preamplifier boards,
 410 which provide a factor of 2333 amplification of the APD
 411 signal.

412 5.2. Layout

413 Similar to the SVT, the ECal is built in two separate
 414 halves that are mirror reflections of one another about
 415 the plane of the nominal electron beam to avoid inter-
 416 fering with the 15 mrad “dead zone”. As shown in Fig-
 417 ure 7, the 221 modules in each half, supported by alu-
 418 minum support frames, are arranged in rectangular for-
 419 mation with five layers and 46 crystals/layer except for
 420 the layer closest to the beam where nine modules were
 421 removed to allow a larger opening for the outgoing elec-
 422 tron and photon beams. Each half was enclosed in a
 423 temperature controlled box ($< 1^\circ\text{ F}$ stability and $< 4^\circ\text{ F}$
 424 uniformity) to stabilize the crystal light yield and the op-
 425 eration of the APDs and its preamplifiers. Four printed
 426 circuit boards mounted on the backplane penetrated the
 427 enclosure and were used to supply the $\pm 5\text{ V}$ operating
 428 voltage for the preamplifiers, 400 V bias voltage to the
 429 APDs, and to read out signals from the APDs. Each half
 430 of the ECal was divided into 12 bias voltage groups with
 431 a gain uniformity of about 20%.

432 During the HPS Test Run, both halves were held in
 433 place by four vertical bars attached to a rail above, plac-
 434 ing the front face of the crystals 147 cm from the up-
 435 stream edge of the magnet, with a 8.7 cm gap between
 436 the innermost edge of the crystals in the two halves.

437 5.3. Signal readout

438 After a 2:1 signal splitter, 1/3 of an amplified APD
 439 signal was fed to a single channel of a JLab flash ADC
 440 (FADC) board [16]. 2/3 of the signal was sent to a
 441 discriminator module and then to a TDC for a timing
 442 measurement. The FADC boards are high speed VXS
 443 modules digitizing up to 16 APD signals at 250 MHz
 444 and storing samples in 8 μs deep pipelines with 12-bit
 445 resolution. When a trigger is received, the part of the
 446 pipeline from 5 samples before and 30 after the signal
 447 which crossed a programmable threshold (for the HPS
 448 Test Run this was set to $\approx 70\text{ MeV}$) are summed and

449 stored in a 17-bit register for readout. In addition a
 450 4 ns resolution timestamp of the threshold crossing is
 451 reported in the readout for each pulse. This scheme
 452 significantly compresses the data output of the FADC.
 453 During offline data analysis, a calibrated pedestal value
 454 is subtracted to obtain the actual summed energy. Two
 455 20-slot VXS crates with 14 (13) FADC boards were em-
 456 ployed in the HPS Test Run to read out the top (bottom)
 457 half of the ECal. In the HPS Test Run 385 out of 442
 458 modules (87%) were used in offline reconstruction, 39
 459 modules were disabled or not read out (no FADC chan-
 460 nel available, no APD bias voltage or masked out due
 461 to excessive noise) and 18 were masked offline due to
 462 noise.

463 6. Trigger and Data Acquisition

464 The DAQ system handles acquisition of data from the
 465 ECal and SVT sub-detectors with two DAQ architec-
 466 tures. The SVT DAQ is based on Advanced Telecom
 467 Communications Architecture (ATCA) hardware while
 468 the ECal uses VMEbus Switched Serial (VXS) based
 469 hardware. Data from the sub-detectors are only read
 470 out when a trigger signal from the trigger system is re-
 471 ceived.

472 6.1. Trigger system

473 The trigger system is designed to select time coinci-
 474 dences of electromagnetic clusters in the top and bot-
 475 tom halves of the ECal. Figure 8 shows a schematic
 476 overview of each stage of the system. Each channel on
 477 the FADC board has an independent data path to send 5-
 478 bit pulse energy and 3-bit pulse arrival time information
 479 every 32 ns to a trigger processing board (CTP), which
 480 is in the same crate. The 3-bit pulse arrival time allows
 481 the trigger to know the pulse timing at 4 ns resolution.
 482 Contrary to the readout path described in Sec. 5.3, this
 483 energy is a pedestal-subtracted time-over-threshold sum

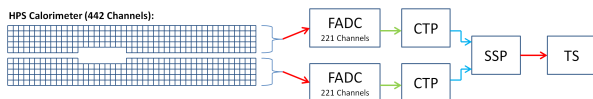


Figure 8: Block diagram of the ECAL trigger system consisting of the FADC that samples and digitizes signals for each detector channel and sends them for cluster finding in the CTP. The CTP clusters are sent to the SSP where the final trigger decision is taken based on pairs of clusters in both halves of the ECal. The decision is sent to the Trigger Supervisor (TS) that generates the necessary signals to read out the sub-detectors.

484 with programmable offsets and minimum threshold dis-
 485 criminator for each channel. With input from all FADC
 486 channels, i.e. one half of the ECal, the CTP performs
 487 cluster finding and calculates cluster energy and tim-
 488 ing information. The 3x3 fixed-window, highly parallel,
 489 FPGA-based cluster algorithm simultaneously searches
 490 for up to 125 clusters with energy sum larger than the
 491 programmable energy threshold (≈ 270 MeV). Crystals
 492 in the fixed-window are included in the sum if the lead-
 493 ing edge of the pulse occurred within a 32 ns time win-
 494 dow to take into account clock skew and jitter through-
 495 out the system. The CTP only accepts clusters with the
 496 locally highest energy 3x3 window to deal with over-
 497 lapsing and very large clusters. The sub-system board
 498 (SSP) receives the clusters from the top and bottom half
 499 CTP at a maximum of 250MHz and searches for pairs
 500 of clusters in an 8 ns wide coincidence window. The
 501 SSP sends triggers to the trigger supervisor (TS), which
 502 generates all the necessary signals and controls the en-
 503 tire DAQ system readout through the trigger interface
 504 units installed in every crate that participate in the read-
 505 out process.

506 The trigger system is free-running and driven by the
 507 250 MHz global clock and has essentially zero dead
 508 time at the occupancies expected for HPS. The trigger
 509 supervisor can apply dead time if necessary, for exam-
 510 ple on a ‘busy’ or ‘full’ condition from the front-end
 511 electronics. The system is designed to handle trigger
 512 rates above 50 kHz and has a latency set to $\approx 3 \mu\text{s}$ to
 513 match that required by the SVT APV25 ASIC. During
 514 the HPS Test Run, for the most part the trigger system
 515 required only a single cluster in either the top or bot-
 516 tom Ecal halves and was tested to trigger rates above
 517 100 kHz by lowering thresholds.

518 6.2. SVT Data Acquisition

519 The SVT DAQ is based on the Reconfigurable Clus-
 520 ter Element (RCE) and cluster interconnect concept de-
 521 veloped at SLAC as generic building blocks for DAQ
 522 systems. The RCE is a generic computational build-
 523 ing block, housed on a separate daughter card called
 524 Data Processing Module (DPM), that is realized on an
 525 ATCA front board called the Cluster On Board (COB),
 526 see Figure 9. The first generation RCE used in the HPS
 527 Test Run consisted of a Virtex 5 FPGA with 1 GB of
 528 DDR3 RAM. A schematic overview of the system is
 529 shown in Figure 10. The analog outputs of up to 12
 530 SVT half-modules (60 APV25 ASICs) are digitized on
 531 the Rear-Transition-Module (RTM), a custom board on
 532 the back side of the ATCA crate, interfacing the HPS-
 533 specific readout to the generic DAQ components on the
 534 COB. A pre-amplifier converts the APV25 differential



Figure 9: The SVT DAQ COB board with four data processing daughter cards (DPMs) visible on the left side.

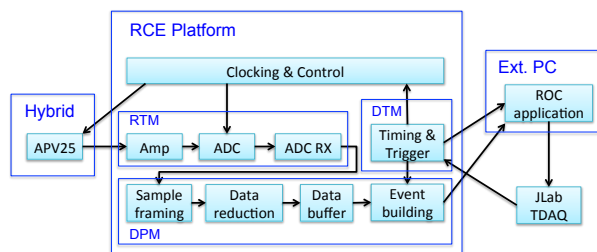


Figure 10: Block diagram overview of the SVT DAQ.

current output to a different voltage output scaled to the sensitive range of a 14-bit ADC operating at the system clock of 41.667 MHz. The RTM is organized into four sections with each section supporting three SVT half-module hybrids (15 APV25 ASICs). The RTM also includes a 4-channel fiber-optic module and supporting logic which is used to interface to the JLab trigger system supervisor. Each section of the RTM is input to a DPM which apply thresholds for data reduction and organizes the sample data into UDP datagrams. The DPM also hosts an I²C controller used to configure and monitor the APV25 ASICs. A single ATCA crate with two COB cards was used, one supporting four DPMs and one supporting three DPMs and one DPM that is configured as the trigger and data transmission module. The two COB cards and their DPMs are interconnected with a 10 Gb/s switch card [17] which also hosts two 1Gb/s Ethernet interfaces to the external SVT DAQ PC.

The external PC supports three network interfaces: two standard 1 Gb/s Ethernet and one custom low-latency data reception card. The first is used for slow control and monitoring of the 8 DPM modules and the second serves as the interface to the JLAB data acquisition system. The third custom low-latency network interface is used to receive data from the ATCA crate and supports a low latency, reliable TTL trigger acknowl-

edge interface to the trigger DPM. This PC hosts the SVT control and monitoring software as well as the Read Out Controller application used to interface with the JLab DAQ.

In order to minimize cable length for the analog APV25 output signal the ATCA crate was located approximately 1 m from the beam line, next to our cable vacuum feed-throughs. Before shielding with lead-blankets was arranged, we observed two failures of normally reliable ATCA crate power supplies, time-correlated to beam instabilities.

Although trigger rates during the HPS Test Run were significantly lower, this system was tested at trigger rates up to 20 kHz and 50 MB/s.

6.3. General Data Acquisition and Online Computing

Every crate participating in the readout process contains a Readout Controller (ROC) that collects digitized information, processes it, and sends it on to the event builder. For the ECal, both VXS crates run ROC applications in a single blade Intel-based CPU module running CentOS Linux OS. For the SVT DAQ, the ROC application runs on the external PC under RHEL. The event builder assembles information from the ROCs into a single event which is passed to the event recorder that writes it to a RAID5-based data storage system capable of handling up to 100 MB/s. The event builder and other critical components run on multicore Intel-based multi-CPU servers. The DAQ network system is a network router providing 10 Gb/s high-speed connection to the JLab computing facility for long-term storage. For the HPS Test Run, both the SVT and ECal ROC had a 1 Gb/s link to the network router.

7. Reconstruction and Performance

7.1. SVT Performance

For the duration of the HPS Test Run all SVT modules and APV25 chips were configured to their nominal operating points [18] with all sensors reverse-biased at 180 V. The sensors were operated within a temperature range of 20 – 24°C. Approximately 97% of the 12,780 SVT channels were found to be operating normally; the fraction of dead or noisy channels varied from 2.4% to 4.7% throughout the HPS Test Run. Most of these losses were due to 2-4 misconfigured APV25 ASICs, a known noisy half-module and problems in two particular APV25 ASICs.

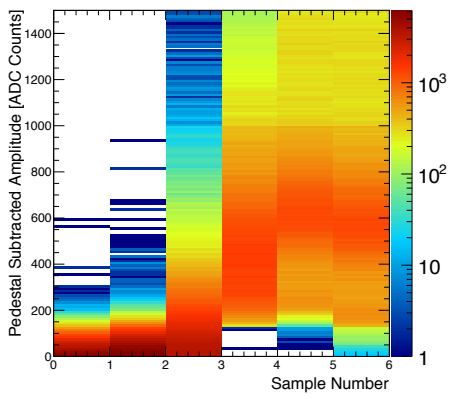


Figure 11: Accumulation of six pedestal-subtracted samples from individual SVT channels associated with hits on tracks.

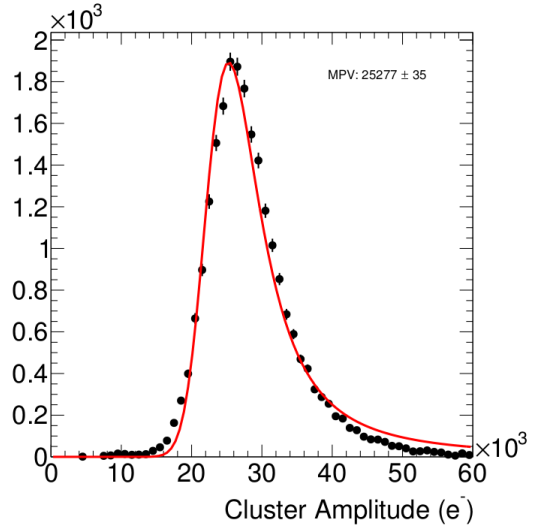


Figure 12: The cluster charge distribution for hits associated with a track follow the characteristic Landau shape.

606 7.1.1. Cluster and Hit Reconstruction

607 After a trigger is received, the amplitude of every
 608 APV25 analogue output is sampled and digitized in
 609 six consecutive time bins, separated by roughly 25 ns.
 610 The typical, pedestal subtracted, pulse shape obtained
 611 is shown in Figure 11. As the figure demonstrates, the
 612 SVT was well timed-in to the trigger with the rise of the
 613 pulse at the 3rd sampling point. In order to find the time,
 614 t_0 , and amplitude of each hit, the six samples from each
 615 channel are fitted to an ideal $CR - RC$ function. Note that
 616 in the HPS Test Run the APV25 ASICs were operating
 617 with a 50 ns shaping time. These hits are passed through
 618 a simple clustering algorithm which forms clusters by
 619 grouping adjacent strips with the position of a cluster on
 620 the sensor determined by the amplitude-weighted mean.
 621 With a linear gain up to ≈ 3 MIPs, the cluster charge
 622 for hits associated with a track follow the characteristic
 623 Landau shape, see Figure 12. A noise level between
 624 $1.1 - 1.5 \times 10^3$ electrons was established through multiple
 625 calibration runs giving a signal to noise ratio of $21 - 25$.
 626 Lab-based radioactive source tests were used to provide
 627 the absolute charge normalization. After clustering hits
 628 on a sensor, the hit time for each cluster is computed as
 629 the amplitude-weighted average of the individually fitted
 630 t_0 on each channel. The t_0 resolution is studied by
 631 comparing the cluster hit time with the average of all
 632 cluster hit times on the track shown in Figure 13. After
 633 correcting for offsets from each sensor (time-of-flight
 634 and clock phase) and accounting for the correlation be-
 635 tween the t_0 and track time, the extracted t_0 resolution is
 636 2.6 ns. This is somewhat worse than the approximately
 637 2 ns resolution expected for S/N=25 which we attribute
 638 to the true pulse shape differing from our idealized fit

639 function which will be improved in the future. Reduc-
 640 ing the APV25 ASIC pulse shaping time to 35 ns will
 641 also improve time resolution. These results show that
 642 we can operate with the six sample readout mode of the
 643 APV25 chip and achieve time resolution adequate for
 644 pileup rejection during electron running in HPS.

645 Good agreement was obtained between observed and
 646 simulated occupancies after taking into account dead or
 647 noisy channels. The hit reconstruction efficiency was
 648 estimated by measuring the number of good tracks with
 649 a hit close to the extrapolated intersection of a given
 650 sensor that was excluded from the track fit itself. Tracks
 651 which intersect regions with known bad channels or
 652 pass very close to the edge region are excluded. The hit
 653 reconstruction efficiency, see Figure 14, was measured
 654 to be above 98% and fairly uniform across the SVT.

655 The spatial resolution of similar microstrip sensors is
 656 well established by test beam data, against which the
 657 charge deposition model in the simulation is validated.
 658 This resolution can be parameterized as a function of the
 659 total signal to single-strip noise and the crossing angle
 660 of tracks through the sensor. The single-hit resolution
 661 for charged particles with signal-to-noise ratio above 20,
 662 as demonstrated here, is relatively constant at approxi-
 663 mately 6 μm for tracks that enter approximately normal
 664 to the sensors as in HPS.

665 7.1.2. Momentum and Vertexing Resolution

666 By selecting e^+e^- pairs from the triggered events we
 667 are able to study basic distributions of pair production

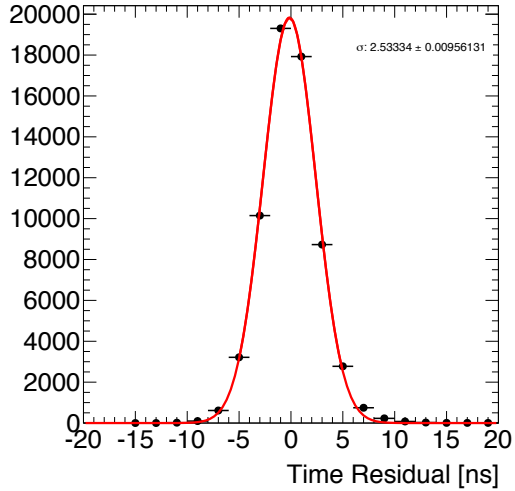


Figure 13: The residual of individual cluster times with the average of all clusters on the track.

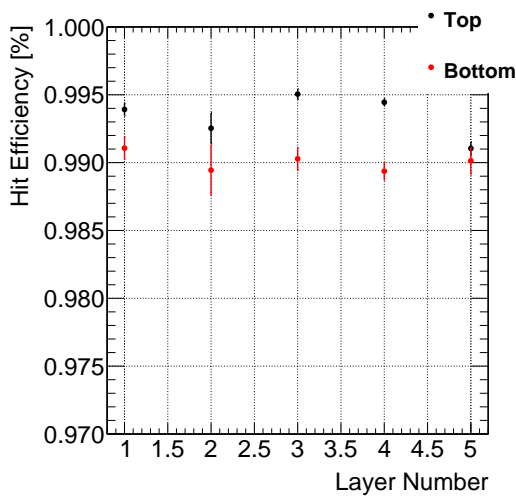


Figure 14: The hit reconstruction efficiency as a function of detector layer.

kinematics. Pairs of oppositely charged tracks, one in the top and one in the bottom half of the SVT, with momentum larger than 400 MeV were selected. The pair production kinematics are relatively well reproduced as shown in Figure 15.

The expected momentum resolution from simulation is between 4-5% for tracks in the momentum range of the HPS Test Run. By comparing, between data and simulation, the shapes of the kinematic distributions for single- and two-track events, we estimate an agreement with the nominal scale and resolution to within 10%.

In the HPS Test Run, as well as in electron running with HPS, the dominant source of uncertainty in the tracking and vertexing is multiple Coulomb scattering. For the vertexing performance the foremost difference compared to electron beam running is that the target was located approximately 67 cm upstream from our nominal target position; giving almost collinear tracks in the detector. The increased lever arm over which tracks are extrapolated widens the resolution with up to a factor of eight (depending on momentum) compared to what is achieved at the nominal electron target position for HPS. Figure 16 shows the horizontal and vertical positions of the extrapolated track at the converter position. While residual alignments show small shifts, the good agreement between data and simulated events of the widths indicates a good understanding of the material budget and distribution in the SVT. Having the dominant contribution to the vertex resolution approximately right demonstrates that the resolution in HPS, with a target at 10 cm, will be as calculated.

7.2. ECal Performance

The integrated pulse of each FADC channel was converted to energy by subtracting a pedestal and applying a conversion factor to convert ADC counts to energy. The pedestals are measured using special runs where each trigger records 100 samples of signals from the APDs with 4 ns between each sample. The pedestals were extracted from the part of the window before the actual hit in the calorimeter. Modules with signal above the threshold are clustered using a simple algorithm similar to the one deployed for the trigger (see Sec. 6.1). Due to the high effective readout threshold of 73 MeV the average number of crystals in a cluster was ~ 3 and the simple clustering algorithm worked well for reconstruction of the detected shower energy. An average noise level of approximately 15 MeV was measured in special pedestal runs.

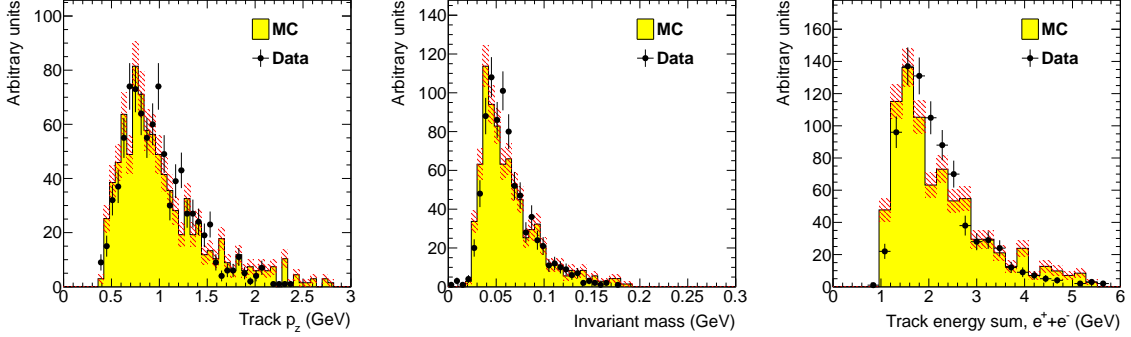


Figure 15: Kinematic distributions for $e^+ e^-$ pairs selected by opposite charged tracks in the top and bottom half of the tracker: track momentum in the top half of the SVT (left), invariant mass (middle) and the sum of the track momentum for the pair (right).

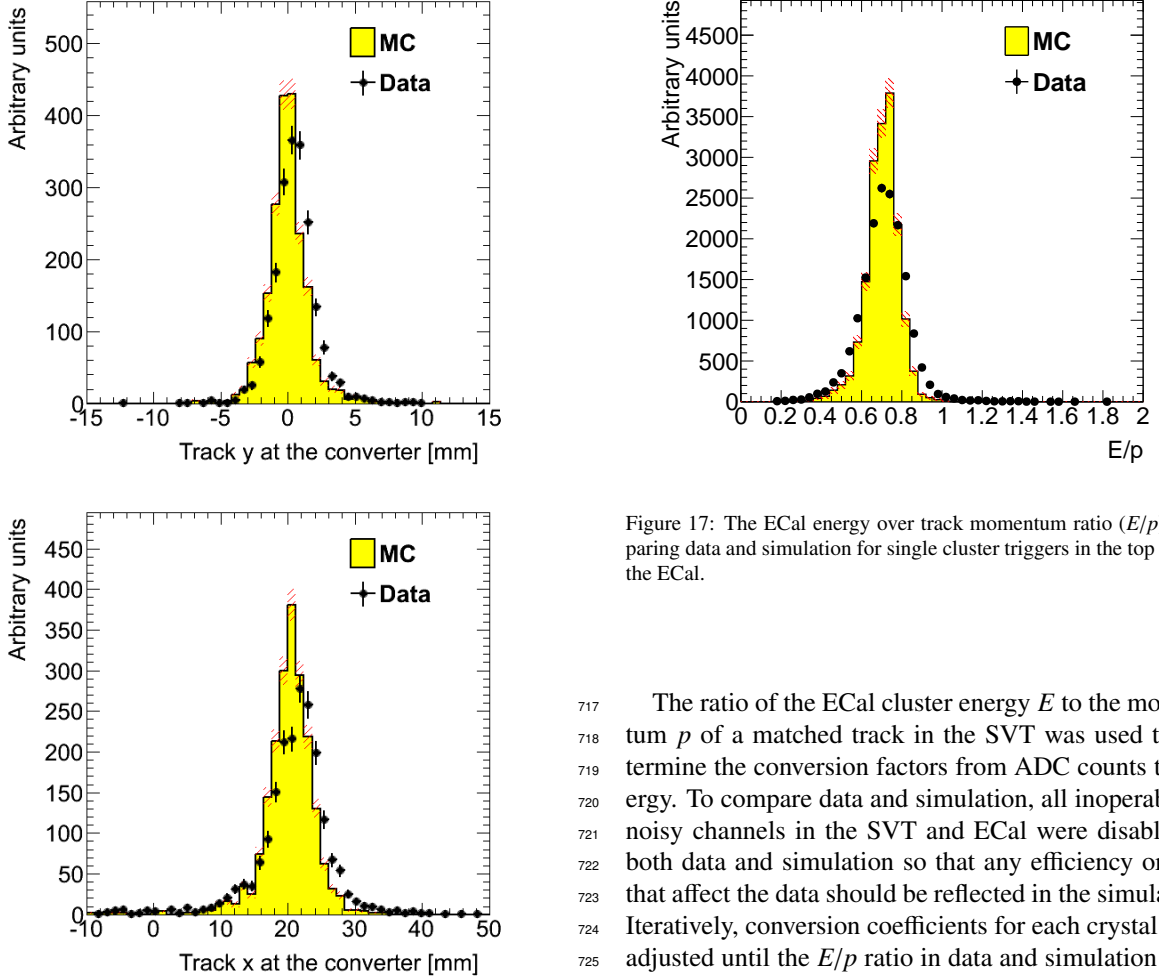


Figure 16: Vertical (top) and horizontal (bottom) extrapolated track position at the converter position taking into account the measured fringe field.

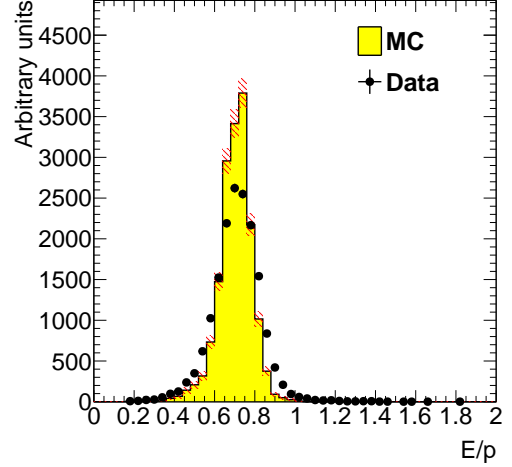


Figure 17: The ECal energy over track momentum ratio (E/p) comparing data and simulation for single cluster triggers in the top half of the ECal.

The ratio of the ECal cluster energy E to the momentum p of a matched track in the SVT was used to determine the conversion factors from ADC counts to energy. To compare data and simulation, all inoperable or noisy channels in the SVT and ECal were disabled in both data and simulation so that any efficiency or bias that affect the data should be reflected in the simulation. Iteratively, conversion coefficients for each crystal were adjusted until the E/p ratio in data and simulation were similar. The distribution of the E/p ratio in data and simulation are compared in Figure 17. The peak position of the distribution indicates the sampling fraction of the ECal, the fraction of the incident particle energy measured in the cluster. The width and tails of the distri-

bution in data indicates imperfect calibration and noise of the ECal modules. This level of calibration and the agreement with simulation was found to be sufficient to study normalized event rates in the HPS Test Run.

7.3. Trigger Performance

As described above in Sec. 6, the energy from each crystal is measured differently in the trigger and what is readout from the ECal. The trigger performance was studied by simulating the trigger for each event and comparing to how the events were actually triggered. To eliminate trigger bias, we use a tag and probe method: to study the trigger performance in one half of the ECal, we select events which triggered the other half and where there was exactly one probe cluster in the ECal half under study. We then measure trigger efficiency as the fraction of tagged events that fired the trigger in the probe half as a function of the probe cluster energy, shown in Figure 18. The trigger turn-on is

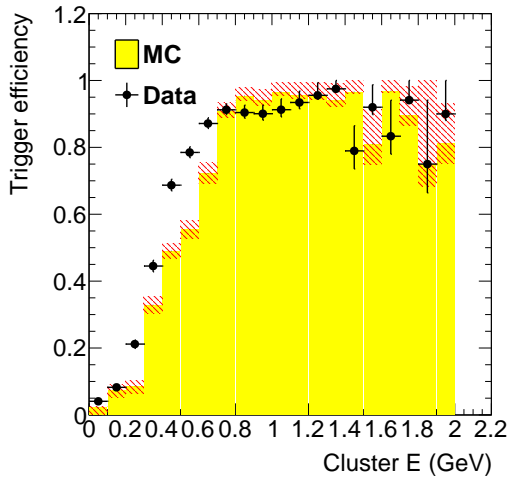


Figure 18: Trigger efficiency in both halves of the ECal for data and simulation as a function of cluster energy.

slow and reaches an uneven plateau just below 1 GeV for two reasons; gain variations between different crystals lead to the threshold variations and the nonlinearity of the time-over-threshold integral means that the effective threshold is higher for clusters that span multiple crystals. The effective trigger threshold is therefore dependent on position and energy of the particle as well as cluster multiplicity.

As a cross-check we simulate the FADC trigger path by converting from readout hits (with fixed-size window integration) to trigger hits (time-over-threshold integration). The CTP clustering algorithm and the trigger

Converter (% X_0)	1.60	0.45	0.18
EGS5	1162 ± 112	255 ± 28	94 ± 17
GEANT4	2633 ± 250	371 ± 38	114 ± 18
Observed	1064 ± 2	196 ± 1	92 ± 1

Table 4: Observed and predicted event rate (in Hz) normalized to 90 nA for three different converter thicknesses. The uncertainty on the prediction includes systematic uncertainties from ECal alignment, background normalization, beam current normalization and limited statistics in the simulation.

decision from the SSP are simulated before we compare the trigger decision and trigger time to what was reported by the actual trigger. For every event, the trigger reports the trigger decision as a bit mask (top half, bottom half or both) and the time the trigger fired. The turn-on from the trigger threshold was measured to be 1280 in units of ADC counts as expected. The threshold was not perfectly sharp because of uncertainties in the conversion from readout to trigger hits described above, but based on comparisons with simulation we found that the trigger worked exactly as specified.

7.4. Trigger Rate Comparisons

Trigger rates observed in the HPS Test Run are dominated by multiple Coulomb scattered e^+e^- pairs in the converter. In simulated events, the rate of triggers depend on the modeling of the pairs' angular distribution and the subsequent multiple Coulomb scattering in the converter. Rates from different converter thicknesses are used to study the varying multiple Coulomb scattering contribution (pair production angle is constant). Restricting clusters to a well calibrated region of the ECal and subtracting the “no converter” background we see agreement with the rates predicted by the EGS5 simulation program, see Table 7.4. This gives further confidence that the dominant source of background occupancy for HPS, multiple Coulomb scattered beam electrons, is well described [19, 20, 21].

8. Summary and Outlook

The HPS Test Run experiment, using a simplified version of the apparatus planned for the full HPS experiment in a parasitic photon beam, demonstrated the feasibility of the detector technologies proposed for the silicon vertex tracker, electromagnetic calorimeter, and data acquisition systems. Performance from each of these subsystems has been shown to be adequate to conduct the full experiment successfully. Studies of multiple Coulomb scattering tails of electrons and positrons from photon conversions further backs expectations from simulation, giving credence to estimates

800 of the detector backgrounds expected in electron beam
801 running for HPS.

802 9. Acknowledgements

803 The authors are grateful for the support from Hall B
804 at JLab and especially the Hall B engineering group for
805 support during installation and decommissioning. They
806 also would like to commend the CEBAF personnel for
807 good beam performance, especially the last few hours
808 of operating CEBAF6. The tremendous support from
809 home institutions and supporting staff also needs praise
810 from the authors.

811 This work has been supported by the US Department
812 of Energy.

- 855 [16] D. H., et al., Integrated tests of a high speed VXS
856 switch card and 250 MSPS flash ADCs, 2007.
857 doi:10.1109/NSSMIC.2007.4436457.
858 [17] R. Larsen, Emerging New Electronics Standards for Physics,
859 Conf.Proc. C110904 (2011) 1981–1985.
860 [18] L. Jones, APV25-S1: User guide version 2.2, RAL Microelec-
861 tronics Design Group, 2011.
862 [19] D. Attwood, P. Bell, S. Bull, T. McMahon, J. Wilson, et al.,
863 The scattering of muons in low Z materials, Nucl.Instrum.Meth.
864 B251 (2006) 41–55.
865 [20] G. Shen, C. Ankenbrandt, M. Atac, R. M. Brown, S. Ecklund,
866 et al., Measurement of Multiple Scattering at 50-GeV/c to 200-
867 GeV/c, Phys.Rev. D20 (1979) 1584.
868 [21] B. Gottschalk, A. Koehler, R. Schneider, J. Sisterson, M. Wag-
869 ner, Multiple coulomb scattering of 160 mev protons, Nuclear
870 Instruments and Methods in Physics Research Section B: Beam
871 Interactions with Materials and Atoms 74 (1993) 467 – 490.

813 References

- 814 [1] B. Holdom, Two U(1)'s and Epsilon Charge Shifts, Phys.Lett.
815 B166 (1986) 196.
816 [2] R. Essig, J. A. Jaros, W. Wester, P. H. Adrian, S. Andreas, et al.,
817 Dark Sectors and New, Light, Weakly-Coupled Particles (2013).
818 [3] M. Pospelov, Secluded U(1) below the weak scale, Phys.Rev.
819 D80 (2009) 095002.
820 [4] O. Adriani, et al. (PAMELA Collaboration), An anomalous
821 positron abundance in cosmic rays with energies 1.5-100 GeV,
822 Nature 458 (2009) 607–609.
823 [5] M. Ackermann, et al. (Fermi LAT Collaboration), Measure-
824 ment of separate cosmic-ray electron and positron spectra with
825 the Fermi Large Area Telescope, Phys.Rev.Lett. 108 (2012)
826 011103.
827 [6] M. Aguilar, et al. (AMS Collaboration), First Result from the
828 Alpha Magnetic Spectrometer on the International Space Sta-
829 tion: Precision Measurement of the Positron Fraction in Pri-
830 mary Cosmic Rays of 0.5350 GeV, Phys.Rev.Lett. 110 (2013)
831 141102.
832 [7] N. Arkani-Hamed, D. P. Finkbeiner, T. R. Slatyer, N. Weiner, A
833 Theory of Dark Matter, Phys.Rev. D79 (2009) 015014.
834 [8] J. D. Bjorken, R. Essig, P. Schuster, N. Toro, New Fixed-Target
835 Experiments to Search for Dark Gauge Forces, Phys.Rev. D80
836 (2009) 075018.
837 [9] A. G. et al. (HPS Collaboration), HPS Heavy Photon Search
838 Proposal, 2010.
839 [10] A. Sandorfi, et al., 2012. URL:
840 http://www.jlab.org/exp_prog/proposals/06/PR-06-101.pdf.
841 [11] I. Rashevskaya, S. Bettarini, G. Rizzo, L. Bosisio, S. Dittongo,
842 et al., Radiation damage of silicon structures with electrons of
843 900-MeV, Nucl.Instrum.Meth. A485 (2002) 126–132.
844 [12] D. S. Denisov, S. Soldner-Rembold, D0 Run IIB Silicon Detec-
845 tor Upgrade: Technical Design Report (2001).
846 [13] M. French, L. Jones, Q. Morrissey, A. Neviani, R. Turchetta,
847 et al., Design and results from the APV25, a deep sub-micron
848 CMOS front-end chip for the CMS tracker, Nucl.Instrum.Meth.
849 A466 (2001) 359–365.
850 [14] M. Friedl, C. Irmler, M. Pernicka, Readout of silicon strip detec-
851 tors with position and timing information, Nucl.Instrum.Meth.
852 A598 (2009) 82–83.
853 [15] A. Radyushkin, P. Stoler (Eds.), Inner Calorimeter in Clas/dvcs
854 Experiment, 2008.